Research Square

Preprints are preliminary reports that have not undergone peer review.
They should not be considered conclusive, used to inform clinical practice,
or referenced by the media as validated information.

Identification and validation of composite performance boundaries for an electro-hydrostatic actuator under multi-source degradation and task loads

tian lan
Zhejiang Sci-Tech University
huanguo chen
Zhejiang Sci-Tech University
shimin feng
Zhejiang Sci-Tech University
hui liu
Beijing Institute of Precision Mechatronics and Controls
peng zhang
Beijing Institute of Precision Mechatronics and Controls
haohan tao
Zhejiang Sci-Tech University
naihao liu
Zhejiang Sci-Tech University
jianwei wu
202210501016@mails.zstu.edu.cn

Zhejiang Sci-Tech University

Research Article

Keywords: Electro-hydrostatic actuator, Multi-source degradation, Gaussian process regression, Task load, Performance boundary, Performance assessment

Posted Date: November 26th, 2026

DOI: https://doi.org/10.21203/rs.3.rs-11794702/v1

License: This work is licensed under a Creative Commons Attribution 4.0 International License.
Read Full License

Additional Declarations: No competing interests reported.

Identification and validation of composite performance boundaries for an electro-hydrostatic actuator under multi-source degradation and task loads

Abstract: Assessing an electro-hydrostatic actuator (EHA) before repeated task execution requires identifying acceptable degradation states under the intended load. This study develops a framework for identifying composite performance boundaries under a prescribed reciprocating actuation task, accounting for pump leakage, reduced controller proportional gain, and external load. AMESim simulations and Gaussian process regression (GPR) relate degradation parameters and task load to maximum displacement-response deviation, steady-state displacement-response deviation, and settling time. A composite performance margin combines the three requirements. Zero-level-set extraction and connected-component selection identify the main acceptable degradation domain connected to the healthy state. The analysis determines governing constraints and their transitions and evaluates load and threshold effects. Independent simulations, AMESim boundary cross-sections, and bench tests validate the performance maps and boundary predictions. Maximum displacement-response deviation and settling time govern different segments of the main composite boundary, whereas steady-state displacement-response deviation does not govern any segment of that boundary. Increasing load from 1000 to 3000 N reduces domain area by approximately 17.5%. Tightening the settling-time threshold by 5% reduces area by approximately 26–29%. Across 15 boundary cross-sections, the boundary-location root mean square error is 0.004527 in normalized degradation coordinates. The predicted task-state classifications agree with the bench-test classifications for all seven cases, although discrepancies remain in the composite performance margins. The framework identifies the principal performance constraints and acceptable degradation range under the specified task conditions, supporting system-level degradation performance assessment.

Keywords: Electro-hydrostatic actuator; Multi-source degradation; Gaussian process regression; Task load; Performance boundary; Performance assessment

1 Introduction

Electro-hydrostatic actuators (EHAs) combine high power density, fast response, and a compact, integrated design. These characteristics are valuable for launch-vehicle attitude and thrust vector control [1–3]. After a reusable launch vehicle completes a flight, ground inspection and assessment must establish whether the EHA can meet the actuation requirements of its next mission. Repeated use can degrade both hydraulic power delivery and closed-loop control. Position feedback can compensate for part of the resulting performance loss, so the condition of an individual component does not directly establish the actuator's ability to perform a task. Assessment before reuse therefore requires identifying, for a given load, the range of degradation states that meet the prescribed requirements and the boundary of that range.

Research on EHA degradation has focused on fault identification, degradation modeling, and reliability assessment. Multi-source data fusion, simulation-assisted learning, and deep learning have been used to identify faults from small samples, distinguish previously unknown faults, and diagnose faults under varying operating conditions [4–8]. Studies of degradation and reliability have examined how multiple degradation processes affect the reliability of closed-loop electrohydraulic systems and have incorporated physical information into EHA degradation models [9–11]. Other studies have analyzed actuator responses to faults and the critical operating conditions of piston pumps [10–12]. For variable loads, robust degradation indicators and physics-informed feature learning have been used to reduce the influence of load on degradation assessment [13, 14]. These studies address changes in system reliability or the robustness of degradation indicators to load

variation. For a closed-loop EHA with both pump leakage and a reduced controller proportional gain, the joint effects of degradation and load on task performance, and the range that remains acceptable under multiple requirements, still require quantitative assessment.

Performance boundary mapping relates system parameters to specified performance requirements [15]. Sequential experimental design, Kriging surrogate models, and adaptive learning have been used to approximate contours and failure boundaries of implicit performance functions [16–18] and to identify limit states and assess reliability in systems with multiple failure modes [19–22]. Gaussian process surrogates have also been used to quantify and propagate uncertainty in EHA performance [23]. Established methods for performance boundary mapping, Kriging surrogate modeling, and reliability analysis with multiple failure modes provide a basis for identifying limit states in complex systems. For a closed-loop EHA subject to multiple sources of functional degradation, the remaining questions are which degradation states are acceptable under the combined load and performance constraints, which constraint governs each part of the boundary, and how that constraint changes with degradation and load. This study uses established surrogate modeling methods to identify the factors that limit actuator-level task performance.

We developed a framework for identifying the composite performance boundary of an EHA under multi-source degradation at different task loads. Pump leakage and controller proportional-gain degradation were modeled in AMESim. GPR then related these two degradation sources and task load to actuator performance. We identified the main acceptable degradation domain under joint performance constraints, examined the effects of load and failure thresholds on its boundary, and evaluated the results using independent simulations, boundary cross-sections, and bench tests. The study makes three contributions to system-level performance assessment under the prescribed test conditions.

(1) A quantitative performance mapping incorporating task load is established for EHA multi-source degradation. GPR characterizes the relationships between piston pump leakage, reduced controller proportional gain, task load, and multiple actuator-level task performance metrics.

(2) Joint constraints on the task metrics identify the main acceptable degradation domain connected to the healthy state. The governing performance constraint and its transition along the composite performance boundary identify the limiting metric for different combinations of degradation levels.

(3) The analysis identifies how task load and performance failure thresholds affect the acceptable degradation range and governing constraints, and provides boundary validation at multiple levels. Domain contraction under changing loads and performance requirements was analyzed. AMESim boundary cross-sections and bench tests were used to validate boundary predictions and task-state classifications.

2 EHA simulation model and performance characterization

2.1 System configuration and degradation characterization

The EHA comprises a position controller, a servomotor, a bidirectional piston pump, a hydraulic circuit, and a hydraulic cylinder (Fig. 1). The controller adjusts motor speed and direction in response to the difference between the actuation command and the measured piston rod displacement. The resulting change in pump flow rate and direction establishes a pressure difference

across the cylinder and moves the rod. The external load affects the actuation response by changing the pressure required.

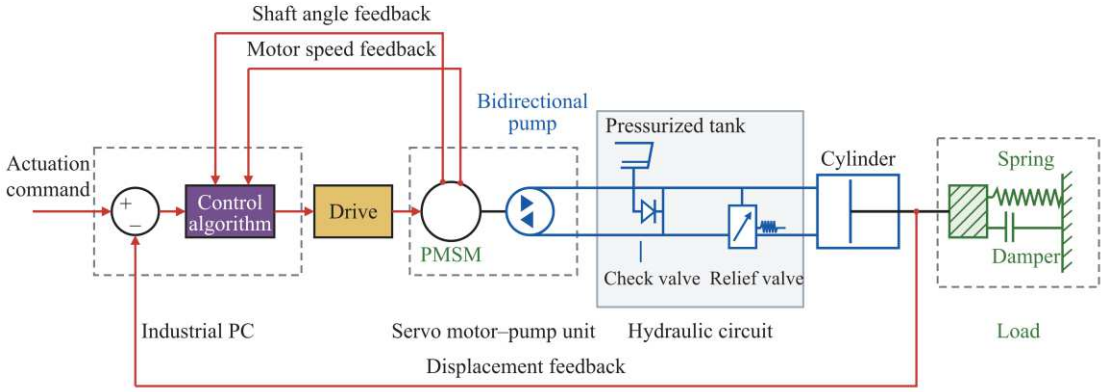


Fig. 1 EHA components and closed-loop control

EHA task performance depends on both hydraulic flow delivery and closed-loop control. Internal pump leakage reduces the flow delivered at a given speed. The position loop can compensate for part of this loss by adjusting motor speed in response to displacement error, so the displacement response can remain close to its healthy counterpart during the early stages of degradation. A further increase in leakage or task load demands more compensation. If the controller's ability to correct errors also declines, displacement and dynamic performance may deteriorate further.

Internal piston pump leakage and controller proportional-gain degradation were selected to represent a loss of hydraulic flow delivery capability and a loss of closed-loop control authority, respectively.

During prolonged operation, wear at the piston–bore and cylinder block–valve plate interfaces can increase internal clearances. Fluid then leaks from the high-pressure side to the low-pressure side, reducing volumetric efficiency (Fig. 2). An equivalent leakage clearance represents the aggregate change in internal leakage paths. For laminar flow through a narrow clearance, the leakage flow rate can be approximated as

$$Q_L = K\frac{\delta^3 \Delta p}{\mu} \tag{1}$$

where Q_L is the leakage flow rate, δ is the equivalent leakage clearance, Δp is the pressure difference across the leakage path, μ is the dynamic viscosity of the fluid, and K is a coefficient determined by the geometry of the equivalent leakage path.

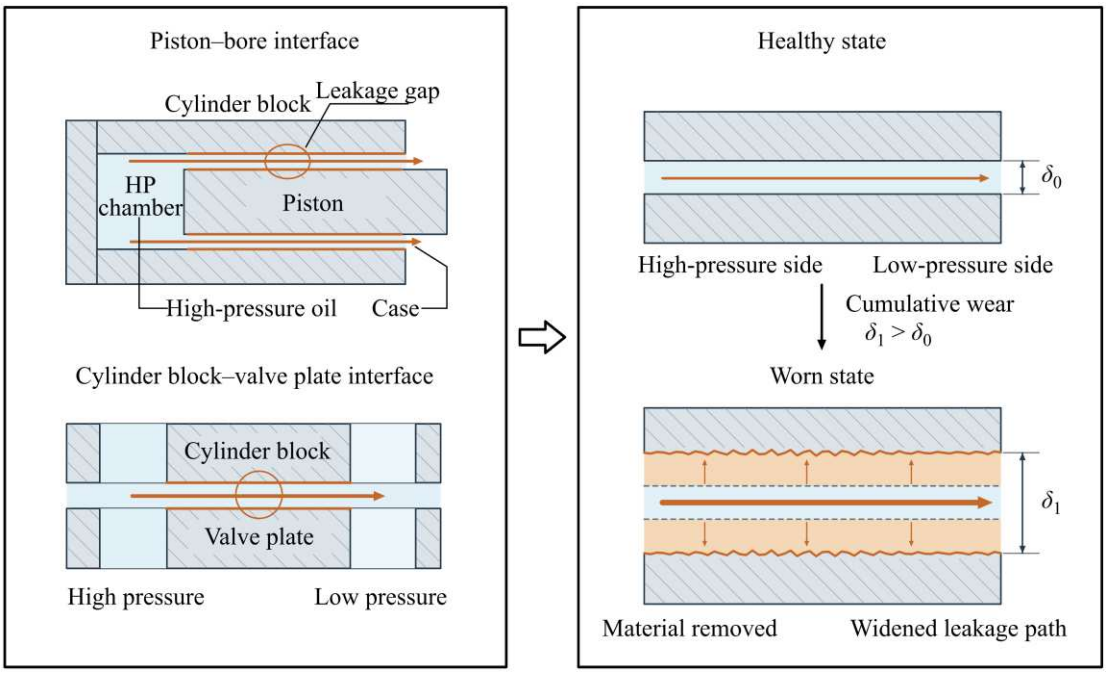


Fig. 2 Mechanism of internal leakage degradation in the piston pump

At comparable pump speed, pressure difference, and fluid viscosity, a larger equivalent clearance increases internal leakage and reduces the effective delivery flow. This can affect pressure buildup and displacement response. The normalized pump leakage degradation parameter is defined as

$$s_L = \frac{\delta}{\delta_{\max}} \tag{2}$$

where $\delta_{\max}$ is the largest leakage clearance in the range considered.

Electronic component aging and parameter drift during prolonged controller operation may alter the gain characteristics of the control channel. This study does not model the specific degradation processes of internal controller components. Instead, a reduction in position-loop proportional gain serves as an equivalent representation of degradation in the controller's regulation capability. The position controller comprises proportional, integral, and filtered derivative branches, and its output is expressed as follows:

$$u(t) = p_g e(t) + u_I(t) + u_D(t) \tag{3}$$

where $u(t)$ is the control output, p_g is the global proportional gain, $e(t)$ is the difference between commanded and measured displacement, and $u_I(t)$ and $u_D(t)$ are the integral and derivative control contributions, respectively.

A reduction in position-loop proportional gain decreases the proportional control component for a given displacement error, thereby changing the position-loop output. After passing through the saturation block, this output becomes the motor speed reference and is combined with actual speed feedback in the speed regulator to generate a torque command. Field-oriented control (FOC) and current control then regulate the motor current, with the q-axis current producing electromagnetic torque to drive motor rotation. Motor speed is influenced by electromagnetic torque, piston-pump

load torque, and mechanical resistance torque. Changes in motor speed in turn alter the theoretical pump delivery flow rate. Meanwhile, the pump load torque acts back on the motor shaft, coupling the motor drive to the hydraulic load. Thus, a reduction in controller proportional gain affects EHA actuation performance through motor speed regulation and hydraulic flow delivery. Fig. 3 illustrates this mechanism.

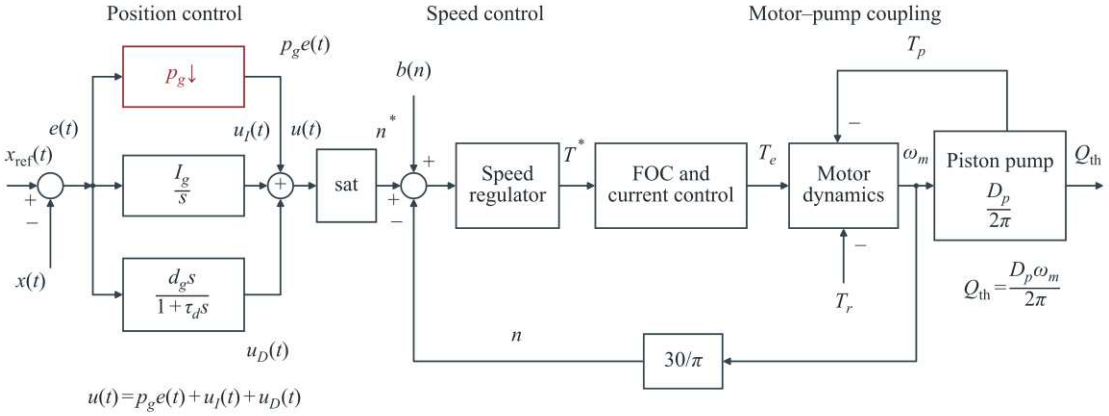


Fig. 3 Mechanism by which position-loop proportional gain degradation affects the EHA drive system

The normalized controller degradation parameter is defined as

$$s_C = \frac{p_{g0} - p_g}{p_{g0} - p_{g,\min}} \tag{4}$$

where p_{g0} is the global proportional gain in the healthy state, $p_{g,\min}$ is the gain at the highest degradation level considered, and p_g is the gain in the current state.

Both s_L and s_C range from 0 to 1. Zero denotes the healthy model state, and 1 denotes the highest degradation level considered.

2.2 EHA simulation model and experimental platform

A closed-loop AMESim model was developed to represent EHA actuation, including the controller, servo motor, bidirectional piston pump, hydraulic circuit, hydraulic cylinder, and external load, as shown in Fig. 4. Pump leakage degradation was simulated using a variable laminar orifice between the hydraulic lines on either side of the piston pump. Its equivalent leakage clearance was adjusted to vary the leakage flow rate. Controller degradation was implemented by reducing the global proportional gain of the position loop. According to the degradation parameter definitions, the corresponding model parameters were set to $\delta = 0.25 s_L$ mm and $p_g = 3700 - 1200 s_C$. Table 1 lists the main model parameters.

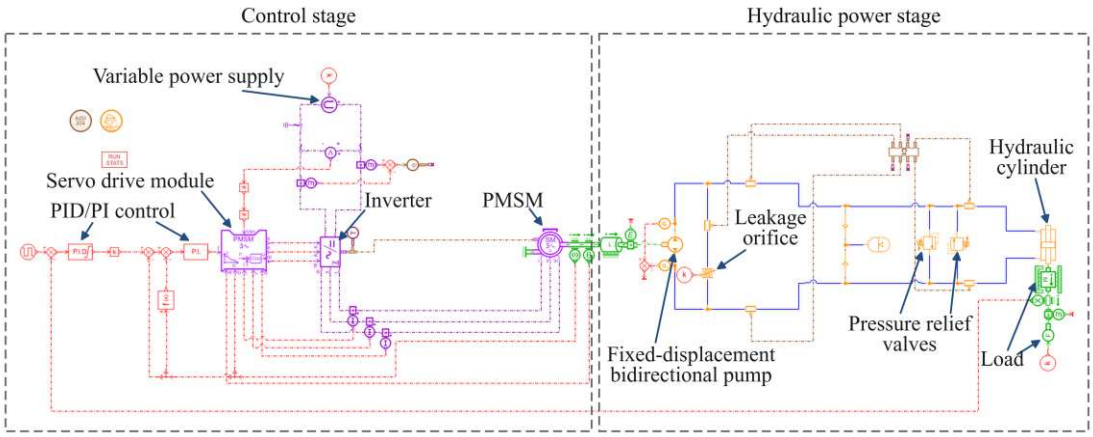
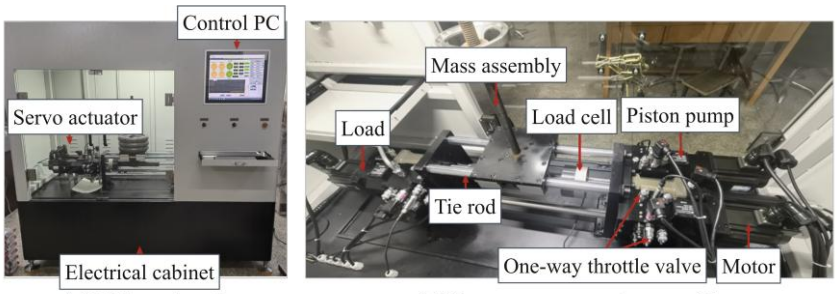


Fig. 4 EHA simulation model

Table 1 Degradation parameters and operating conditions

Parameter	Value or range	Unit
Nominal piston pump displacement	1.6	mL/rev
Maximum hydraulic cylinder stroke	120	mm
Relief valve pressure setting	20	MPa
Pump leakage degradation parameter	0~1	—
Maximum leakage clearance	0.25	mm
Controller degradation parameter	0~1	—
Global proportional gain	3700~2500	—
Load	1000/2000/3000	N
Simulation duration	60	s
Sampling interval	0.002	s

The EHA performance degradation test platform comprises an industrial control computer, an electrical control system, an EHA, and a loading device, as shown in Fig. 5. Servo motor speed, piston-pump differential pressure, and actuator displacement were measured during the tests. Table 2 lists the main parameters. Pump-side degradation was introduced by adjusting the opening of the bypass one-way throttle valve to vary leakage flow and simulate reduced hydraulic flow delivery capability. Controller degradation was introduced by reducing the position-loop proportional gain K_p. The bench and AMESim proportional gains satisfy the numerical relationship $p_g = 1000K_p$, with healthy-state values of 3.70 and 3700, respectively.



(a) EHA test bench

(b) Key components and pump-side degradation injection site

Fig. 5 EHA performance degradation test platform and key components

Table 2 Parameters of the EHA degradation test bench

Parameter	Value
Rated EHA operating pressure (MPa)	17
Rated servo motor power (kW)	1.5
Nominal piston pump displacement (mL/rev)	1.6
Maximum actuator stroke (mm)	120
Inertial load mass (kg)	30
Proportional gain	3.7

The bench bypass and the simulated internal pump leakage follow different flow paths. Both reduce the effective flow available to the actuator, thereby affecting its actuation performance. Their equivalence is defined at the system level in terms of available flow. The quantitative correspondence was established by calibration.

2.3 Task conditions and performance evaluation method

A periodic step displacement command reproduced a typical reciprocating bench task and provided a common test for the combined effects of degradation and external load. The command switched between 0 and 60 mm with a period of 20 s and a 50% duty cycle. Each 60 s simulation covered three full cycles, comprising three extension strokes and three retraction strokes. Results were recorded every 0.002 s. The external load applied at the cylinder output was independently set to 1000, 2000, or 3000 N and held constant throughout each test.

Three task-level metrics characterized displacement departure, steady-state holding accuracy, and dynamic convergence: maximum displacement-response deviation, steady-state displacement-response deviation, and settling time. The first two quantify the change from the healthy displacement response under the same load, rather than absolute tracking error relative to the command. Settling time uses the steady-state position of the healthy response under the same load as its reference. Each metric was evaluated separately for the six strokes, and the worst value was retained for the case.

(1) Maximum displacement-response deviation

For a given stroke, maximum displacement-response deviation is the largest absolute difference between the degraded and healthy responses under the same load:

$$e_{\max} = \max_{t\in[t_a,t_b]} \left| x_d(t) - x_h(t) \right| \tag{5}$$

where $x_d(t)$ and $x_h(t)$ denote the degraded and healthy displacement responses under the same load, and t_a and t_b are the start and end times of the stroke.

(2) Steady-state displacement-response deviation

The steady-state evaluation window covers the final 20% of each stroke. Steady-state displacement-response deviation is the mean pointwise absolute difference between the degraded and healthy responses under the same load over this window:

$$e_{ss} = \frac{1}{N}\sum_{i=1}^{N}\left|x_d(t_i) - x_h(t_i)\right| \tag{6}$$

where N is the number of samples in the steady-state window and t_i is the time of its ith sample.

(3) Settling time

For each stroke, the median displacement over the final 20% of the healthy response under the same load defines the center of a tolerance band with a half-width of 3 mm. Settling time is the elapsed time until the degraded response first enters the band and remains there until the end of the stroke:

$$t_s = t_{in} - t_0, \tag{7}$$

Here, t_{in} is the earliest time satisfying

$$|\, x_d(t) - x_{h,ss} \,| \le 3\ \text{mm}, \quad \forall t \in [t_{\text{in}}, t_b] \tag{8}$$

where $x_{h,ss}$ is the median displacement in the final 20% of the corresponding healthy stroke under the same load, and t_0 and t_{b} are the start and end times of the current stroke.

If the response fails to enter the band and remain there until the end of any stroke, the case fails the settling-time requirement. It is classified as a task performance failure and is not assigned a continuous settling-time value.

For the prescribed task, joint performance constraints were imposed on maximum displacement-response deviation, steady-state displacement-response deviation, and settling time. Their respective failure thresholds were 6 mm, 3 mm, and 6.5 s (Table 3).

Table 3 Task performance failure thresholds

Performance metric	Symbol	Failure threshold
Maximum displacement-response deviation	H_e	6 mm
Steady-state displacement-response deviation	H_{ss}	$3mm$
Settling time	H_{t_s}	6.5 s

A degradation state fails the test if any metric exceeds its threshold. It is acceptable if all three metrics are at or below their thresholds. Failure to settle within a prescribed stroke also makes the state unacceptable. Eq. (9) gives the joint criterion.

$$e_{\max} > H_e \quad \text{or} \quad e_{ss} > H_{ss} \quad \text{or} \quad t_s > H_{t_s} \tag{9}$$

Performance failure here pertains to the prescribed test and its thresholds. Application to a specific launch vehicle requires checking these thresholds against the mission command, absolute

tracking accuracy, and dynamic response requirements before using the domain or its boundary for mission acceptance.

2.4 Model validation and leakage parameter calibration

To evaluate the AMESim model's ability to represent the basic EHA dynamic response, simulated and measured responses were compared under identical periodic step-displacement tasks and operating conditions. The comparison covered servo motor speed, piston-pump differential pressure, and actuator displacement. Fig. 6 shows the responses, and Table 4 summarizes the errors.

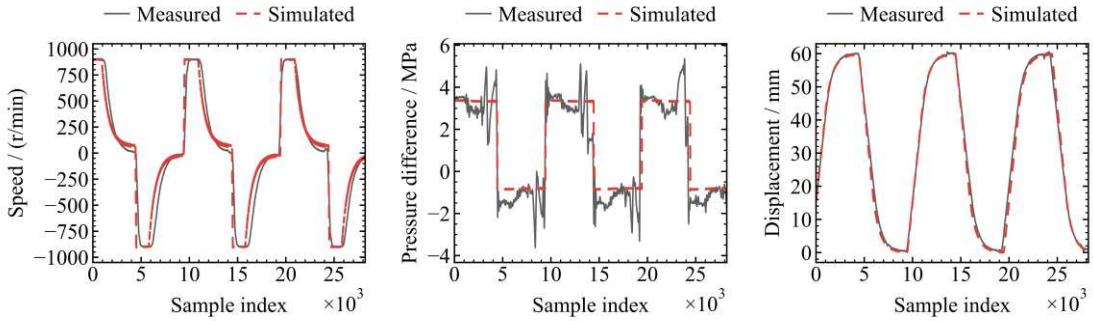


Fig. 6 Comparison of simulated and measured responses under a periodic step-displacement task

Table 4 Differences between simulated and measured responses

Response variable	MAE	RMSE	95th percentile of absolute error	Correlation coefficient
Servo motor speed (rev/min)	115.8	204.5	405.0	0.933
Piston pump pressure difference (MPa)	0.57	0.88	1.76	0.937
Actuator displacement (mm)	1.24	1.87	4.28	0.997

Fig. 6 and Table 4 show close agreement between the overall simulated and measured response trends. For actuator displacement, the correlation coefficient was 0.997 and the root mean square error (RMSE) was 1.87 mm. Local speed and differential-pressure discrepancies mainly occurred during direction reversals and rapid pressure changes. These discrepancies may be associated with the actual system's damping characteristics, drive dynamics, and measurement disturbances. The results indicate that the AMESim model adequately represents the principal closed-loop actuation characteristics under the measured conditions. They do not directly establish the same accuracy for other combinations of degradation state and load.

To relate bench bypass leakage to the internal pump leakage parameter in the simulation, an index of effective flow delivery capability was used for calibration. For a fixed-displacement piston pump during steady actuation, transient flow changes due to fluid compressibility and energy stored in the lines were neglected. The flow continuity relation can then be approximated as

$$Q_t = Q_a + Q_l \tag{10}$$

with

$$Q_t = \frac{D|n|}{60}, \qquad Q_a = A|\dot{x}| \tag{11}$$

where Q_t is the theoretical pump delivery flow, Q_a is the effective flow driving the cylinder, Q_l is the equivalent flow loss, D is the fixed pump displacement, A is the effective cylinder area, n is motor speed, and $\dot{x}$ is actuator velocity.

Combining Eqs. (10) and (11) for nonzero motor speed gives

$$\frac{|\dot{x}|}{|n|} = \frac{D}{60A} - \frac{Q_l}{A|n|} \tag{12}$$

With pump displacement and effective cylinder area fixed, the ratio of the magnitudes of actuator velocity and motor speed decreases as relative flow loss increases. This ratio defines the flow delivery capability index VE:

$$VE = \frac{|\dot{x}|}{|n|} \tag{13}$$

Bench and simulation results were matched at the same load. A half-turn adjustment of the one-way throttle valve was assigned a nominal opening of 2%. Eight leakage settings covered nominal openings from 1% to 8% in increments of 1 percentage point. Actuator displacement and motor speed were recorded at each setting under 1000, 2000, and 3000 N. The mean of VE was calculated over steady portions of the strokes to reduce the influence of reversals, acceleration, and deceleration. Taking the measured VE as the reference, we calculated the absolute relative error in VE at each load and combined the three errors as an equally weighted root mean square. Minimizing this aggregate matching error determined the pump leakage degradation parameter for each valve opening (Table 5).

Table 5 Calibration of the model pump leakage parameter against bench leakage settings

Nominal throttle valve opening (%)	Pump leakage degradation parameter, s_L	Equivalent leakage clearance, δ (mm)	Combined error (%)
1	0.5162	0.1291	0.306
2	0.6401	0.1600	0.788
3	0.7247	0.1812	1.434
4	0.7911	0.1978	2.254
5	0.8345	0.2086	3.572
6	0.8763	0.2191	5.104
7	0.9170	0.2292	6.360
8	0.9496	0.2374	7.232

Each of the eight openings corresponded to a pump leakage degradation parameter s_L, which increased from 0.5162 to 0.9496 with valve opening (Table 5). The index VE thus related the bench leakage settings to the simulation parameter. The aggregate matching error across the three loads ranged from 0.306% to 7.232% and increased at higher leakage settings. At high leakage and high load, differences between the nonlinear flow–pressure characteristics of bypass and internal leakage became more pronounced, making it difficult to match VE across loads with a single degradation parameter.

3 EHA multi-source degradation performance mapping and validation

GPR was used to establish a quantitative mapping from EHA multi-source degradation states and task loads to system-level task performance. This mapping was then used to identify composite boundaries under joint performance constraints. Fig. 7 presents the overall research framework.

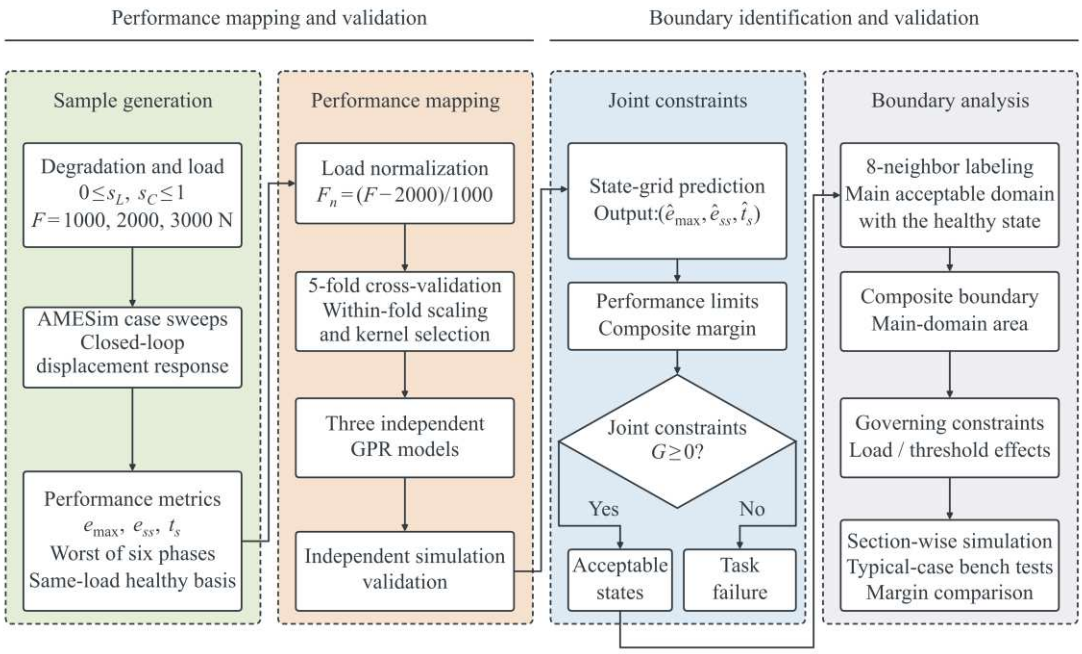


Fig. 7 Framework for EHA multi-source degradation performance mapping and composite boundary identification

3.1 Construction of multi-source degradation simulation samples

The sample variables were the pump leakage degradation parameter s_L, the controller degradation parameter s_C, and the external load F. Both degradation parameters ranged from 0 to 1 in increments of 0.1. A full factorial design at 1000, 2000, and 3000 N gave 363 candidate cases. All other simulation parameters were held constant. Nine cases at 3000 N did not finish within the computational time limit, leaving 354 complete simulations. Table 6 gives the distribution by load.

Table 6 Distribution of degradation simulations by load

Load (N)	Candidate cases	Completed cases	Timed-out simulations
1000	121	121	0
2000	121	121	0
3000	121	112	9
Total	363	354	9

All 354 completed simulations yielded valid values of both maximum and steady-state displacement-response deviation. Ten did not satisfy the settling criterion and had no continuous settling-time value. Each displacement model was therefore trained on 354 cases and the settling-time model on the remaining 344 valid cases.

3.2 GPR performance mapping model construction and training

Separate GPR models were constructed for maximum displacement-response deviation, steady-state displacement-response deviation, and settling time. Each used pump leakage

degradation, controller degradation, and task load as inputs. To place the inputs on comparable scales, load was normalized and the input vector was defined as

$$F_n = \frac{F - 2000}{1000}, \qquad \mathbf{x} = [s_L, s_C, F_n]^{\mathrm{T}} \tag{14}$$

where F_n is the normalized load. Loads of 1000, 2000, and 3000 N correspond to F_n values of −1, 0, and 1, respectively.

The input and output variables were standardized before training:

$$\tilde{z} = \frac{z - \mu_z}{\sigma_z} \tag{15}$$

where μ_z and σ_z are the mean and standard deviation of the variable in the modeling sample. For a standardized input $\tilde{\boldsymbol{x}}$, the performance response function was represented by a Gaussian process:

$$f(\tilde{\boldsymbol{x}}) \sim \mathrm{GP}\left[m(\tilde{\boldsymbol{x}}), k(\tilde{\boldsymbol{x}}, \tilde{\boldsymbol{x}}') \right] \tag{16}$$

where $m(\tilde{\boldsymbol{x}})$ is the mean function and $k(\tilde{\boldsymbol{x}}, \tilde{\boldsymbol{x}}')$ is the covariance function.

Separate length scales l_L, l_C, and l_F allowed the response to vary differently with pump leakage, controller degradation, and load. The distance between two standardized input states was defined as

$$r = \sqrt{\frac{(\tilde{s}_L - \tilde{s}_L')^2}{l_L^2} + \frac{(\tilde{s}_C - \tilde{s}_C')^2}{l_C^2} + \frac{(\tilde{F}_n - \tilde{F}_n')^2}{l_F^2}} \tag{17}$$

Three covariance functions were considered: the radial basis function (RBF), Matérn-3/2, and Matérn-5/2 kernels:

$$\begin{aligned} k_{\mathrm{RBF}}(r) &= \sigma_f^2 \exp\left(-\frac{r^2}{2} \right) \\ k_{\mathrm{M32}}(r) &= \sigma_f^2 (1 + \sqrt{3} r) \exp(-\sqrt{3} r) \\ k_{\mathrm{M52}}(r) &= \sigma_f^2 \left(1 + \sqrt{5} r + \frac{5 r^2}{3} \right) \exp(-\sqrt{5} r) \end{aligned} \tag{18}$$

Here, σ_f^2 is the signal variance. A fixed regularization term of 10^{-6} was added to the diagonal of the kernel matrix for numerical stability. It was not interpreted as physical observation noise.

Five-fold cross-validation compared the three kernels for each performance metric using identical folds for the candidate models. Each fold used only its training subset to estimate standardization parameters and model hyperparameters. Because validation cases had neighboring training cases at the same load, cross-validation primarily measured local interpolation accuracy within the training grid.

The three input length scales and signal variance were optimized during training. The coefficient of determination (R^2), RMSE, and mean absolute error (MAE) were used to assess the models. Table 7 gives the cross-validation results.

Table 7 Cross-validation results for GPR models with different covariance kernels

Performance metric	Kernel	Samples	R^2	RMSE	MAE
e_{max}	RBF	354	0.999951	0.0526	0.0284
e_{max}	Matérn-3/2	354	0.999973	0.0378	0.0223
e_{max}	Matérn-5/2	354	0.999968	0.0406	0.0226
e_{ss}	RBF	354	0.999982	0.0095	0.0035
e_{ss}	Matérn-3/2	354	0.999935	0.0168	0.0067
e_{ss}	Matérn-5/2	354	0.999970	0.0158	0.0045
t_s	RBF	344	0.999993	0.0023	0.0016
t_s	Matérn-3/2	344	0.999972	0.0046	0.0027
t_s	Matérn-5/2	344	0.999992	0.0024	0.0017

Cross-validation favored the Matérn-3/2 kernel for maximum displacement-response deviation and the RBF kernel for both steady-state displacement-response deviation and settling time. After kernel selection, each final model was fitted using all valid training samples for its metric. Table 8 lists the fitted parameters.

Table 8 GPR parameters for the three performance metrics

Performance metric	Kernel	l_L	l_C	l_F	σ_f
e_{max}	Matérn-3/2	3.937	100.00	10.575	9.25
e_{ss}	RBF	0.610	16.04	0.090	11.27
t_s	RBF	0.755	5.96	0.201	5.77

3.3 Independent validation of mapping models

Independent validation used 95 AMESim cases excluded from training: 20 at 1000 N, 55 at 2000 N, and 20 at 3000 N. Each combination of s_L, s_C, and F differed from all training combinations. Both displacement metrics were available for all 95 cases. Six responses did not meet the settling criterion, so continuous settling-time prediction errors were evaluated on the remaining 89 cases.

Fig. 8 compares the GPR predictions and AMESim results for the three performance indicators. Table 9 presents the quantitative independent validation results.

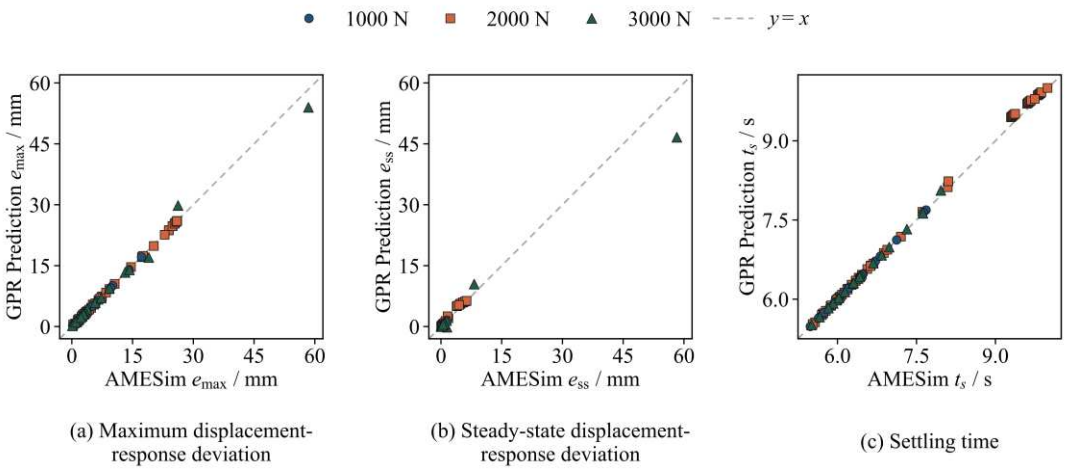


Fig. 8 Comparison of GPR predictions and AMESim results for the three performance indicators

Table 9 Independent validation of the GPR performance maps

Performance metric	Valid samples	R^2	RMSE	MAE
Maximum displacement-response deviation	95	0.9964	0.63mm	0.20mm
Steady-state displacement-response deviation	95	0.9566	1.28mm	0.35mm
Settling time	89	0.9989	0.05s	0.02s

The independent tests showed close agreement for maximum displacement-response deviation and settling time. For steady-state displacement-response deviation, the RMSE was 1.28 mm. Approximately 90% of the total squared prediction error arose from two severely degraded, failed cases far from the main composite performance boundary. The model therefore incurred substantial local errors for this metric in some severely degraded states. Aggregate regression accuracy does not establish boundary location accuracy; the AMESim boundary cross-sections examined below assess errors near critical states.

4 Identification and validation of EHA degradation-state boundaries under multiple performance constraints

4.1 Composite performance boundary identification and governing constraint analysis

To determine which degradation combinations met the task requirements, each of the three performance metrics was normalized against its failure threshold to define a performance margin:

$$g_i(\mathbf{x}) = 1 - \frac{\hat{y}_i(\mathbf{x})}{H_i}, \quad i = 1, 2, 3 \tag{19}$$

Here, $\hat{y}_i$ and H_i are the GPR prediction and failure threshold for metric i. The indices i = 1, 2, and 3 denote maximum displacement-response deviation, steady-state displacement-response deviation, and settling time, respectively. The conditions $g_i > 0$, $g_i = 0$, and $g_i < 0$ indicate that the metric is below, at, or above its threshold.

At a given load, the degradation boundary associated with constraint i is

$$g_i(\mathbf{x}) = 0, \qquad i = 1, 2, 3 \tag{20}$$

The EHA must satisfy all three requirements to complete the prescribed task. The composite performance margin is therefore defined as

$$G(\mathbf{x}) = \min\left[g_1(\mathbf{x}), g_2(\mathbf{x}), g_3(\mathbf{x})\right] \tag{21}$$

When $G \geq 0$, all three metrics meet their requirements, with $G = 0$ denoting a critical state. When $G < 0$, at least one metric exceeds its failure threshold. For a fixed normalized load F_n, the acceptable degradation domain is

$$\Omega(F_n) = \left\{(s_L, s_C) \middle| \; G(s_L, s_C, F_n) \geq 0\right\} \tag{22}$$

An equally spaced 801 × 801 grid was constructed in the degradation parameter space, and acceptable nodes were classified using the composite performance margin. Eight-neighbor connected-component labeling was then applied. The connected region containing the healthy state was defined as the main acceptable degradation domain, while other disconnected acceptable regions were excluded from this domain. Fig. 9 illustrates the identification procedure.

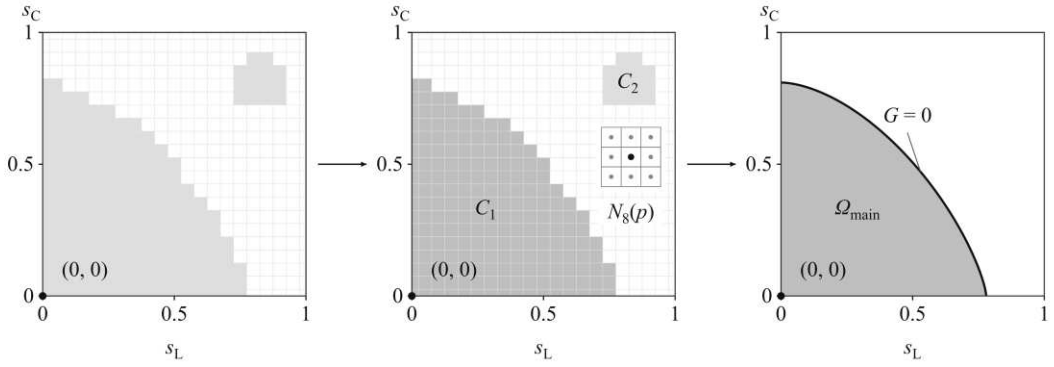


Fig. 9 Identification of the main acceptable degradation domain

The critical performance boundary of the main acceptable degradation domain is defined as

$$\Gamma(F_n) = \left\{(s_L, s_C) \in \partial\Omega_{\text{main}}(F_n) \middle| \; G(s_L, s_C, F_n) = 0\right\} \tag{23}$$

where $\partial\Omega_{\text{main}}(F_n)$ denotes the boundary of the main acceptable degradation domain. The zero-contour segments adjacent to the labeled main domain were retained to obtain the main composite performance boundary.

The zero-level sets of the three performance margin functions were extracted in the degradation-state plane to obtain individual performance boundaries under different loads, as shown in Fig. 10.

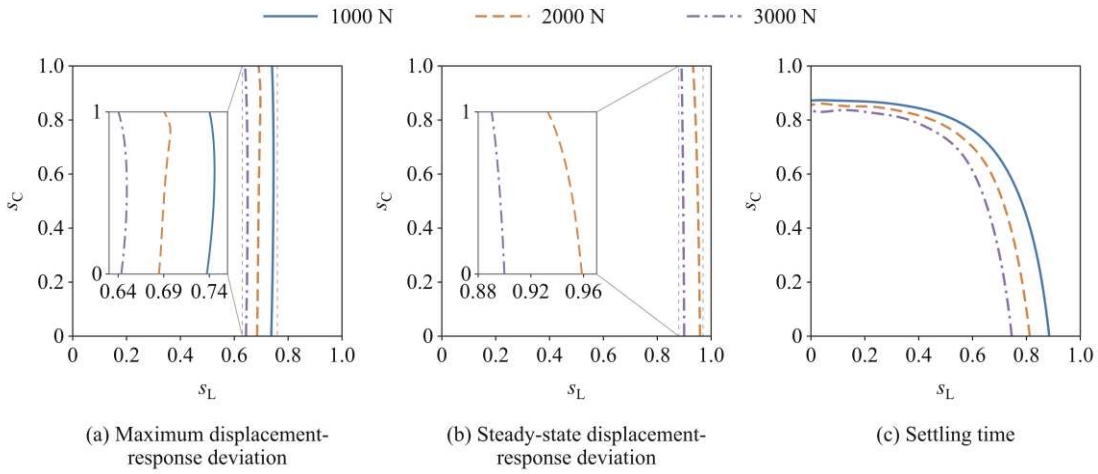


Fig. 10 Degradation-state boundaries under individual performance constraints at different loads

In Fig. 10(a), the maximum displacement-response deviation boundary varies little with controller degradation and is primarily influenced by pump leakage degradation. Increased pump leakage reduces effective flow delivery, affecting pressure buildup and the displacement response of the hydraulic cylinder. Closed-loop regulation cannot fully compensate for transient flow losses during actuation, thereby increasing the maximum displacement-response deviation. As the load increases, the critical boundary shifts toward lower levels of pump leakage degradation.

In Fig. 10(b), the steady-state displacement-response deviation does not reach the 3 mm failure threshold under a load of 1000 N. Boundaries form only at relatively high pump leakage degradation levels under loads of 2000 and 3000 N. This indicator is referenced to the healthy-state response under the same load and reflects degradation-induced changes in displacement response at the end of each motion segment. Under the current closed-loop control configuration, some leakage-degraded conditions exhibit relatively large transient displacement-response deviations, while their end-of-segment responses remain close to the healthy-state response. Thus, the steady-state displacement-response deviation does not increase in parallel with the transient deviation.

In Fig. 10(c), the settling-time boundary varies with both degradation parameters. Reduced controller proportional gain weakens feedback regulation and slows displacement-response convergence. Increased pump leakage reduces effective flow delivery and delays entry into the steady-state tolerance band. The combined effects of these two degradation sources produce a distinctly curved settling-time boundary. Increasing the load further reduces the range of degradation states that satisfy the settling-time requirement.

To compare critical degradation levels across loads, representative values for the individual boundaries were extracted on the $s_C = 0$ and $s_L = 0$ sections (Table 10).

Table 10 Representative critical degradation parameters on individual performance boundaries at each load

Load (N)	Critical s_L for maximum displacement-response deviation	Critical s_L for steady-state displacement-response deviation	Critical s_C for settling time
1000	0.7373	No boundary	0.8717
2000	0.6847	0.9587	0.8545

Load (N)	Critical s_L for maximum displacement-response deviation	Critical s_L for steady-state displacement-response deviation	Critical s_C for settling time
3000	0.6434	0.8999	0.8362

With increasing load, the critical degradation levels decrease for maximum displacement-response deviation and settling time (Table 10). A steady-state displacement-response deviation boundary occurs only at higher loads and substantial pump leakage. The acceptable range contracts as load increases, and the three metrics impose different constraints in the degradation plane. A single metric therefore cannot characterize the full task performance boundary under multi-source degradation.

At each point on the composite performance boundary, the metric with the smallest normalized margin defines the governing performance constraint:

$$j^* = \arg\min_{j\in\{1,2,3\}} g_j(\mathbf{x}) \tag{24}$$

Here, j^* denotes the governing performance constraint at the current boundary location. Where adjacent composite boundary segments are governed by different performance constraints, their junction defines the transition point between governing constraints. Fig. 11 shows the resulting composite degradation-state boundaries under different loads.

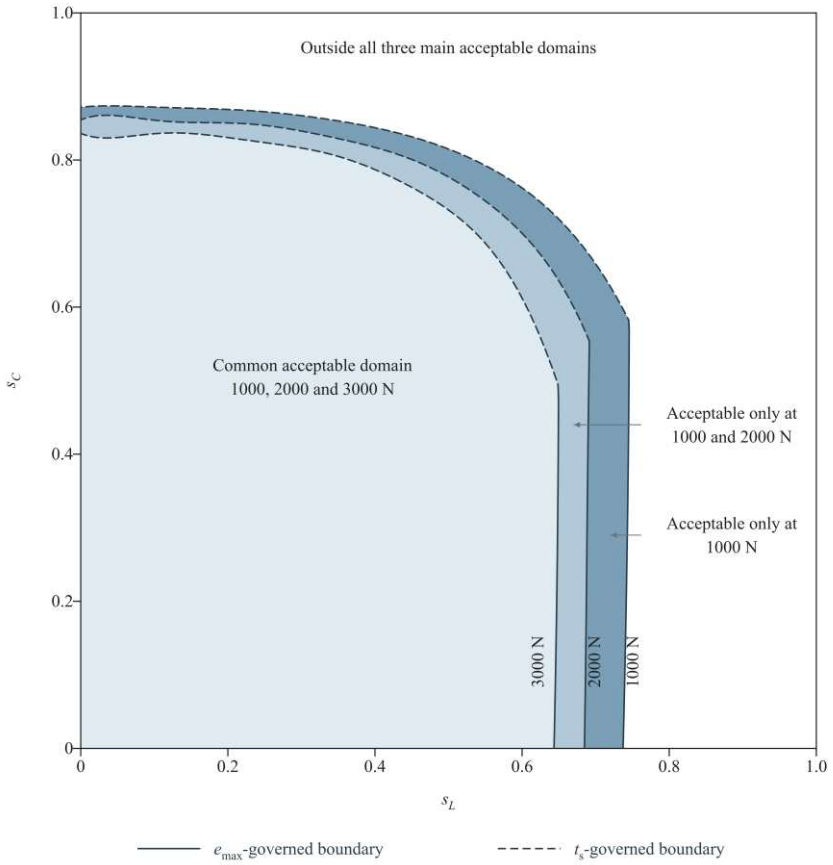


Fig. 11 Main acceptable degradation domains and governing performance boundaries under different loads

Fig. 11 shows that the composite boundary consists primarily of segments governed by the maximum displacement-response deviation and settling-time constraints. The governing constraint changes with the degradation combination. At low controller degradation levels, increased pump leakage reduces effective hydraulic flow delivery and affects displacement buildup following a step command. The maximum displacement-response deviation reaches its failure threshold first and therefore constitutes the principal performance limitation in this region. As controller proportional gain decreases, the proportional control action for a given displacement error weakens. The system response then requires more time to enter and remain within the steady-state tolerance band. When settling time reaches its failure threshold before the other indicators, the settling-time constraint governs the composite boundary. Thus, transitions in the governing constraint reflect changes in the system's dynamic performance limitations across degradation combinations.

Load also affects the relationship between degradation and actuator performance. Higher loads increase the pressure demand and may increase leakage losses at a given clearance, making displacement more sensitive to available flow. The main acceptable degradation domain contracted from an area of 0.6066 at 1000 N to 0.5003 at 3000 N, a reduction of 17.52%. With the present model and thresholds, increasing load predominantly contracted the acceptable range. Maximum displacement-response deviation and settling time continued to govern distinct boundary segments.

The fraction of main boundary arc length governed by each constraint was defined as

$$p_j = \frac{L_j}{L_\Gamma} \times 100\% \tag{25}$$

where L_j is the arc length governed by constraint j and L_Γ is the total arc length of the main composite performance boundary. Table 11 gives the results by load.

Table 11 Percentage of composite performance boundary arc length governed by each constraint

Load (N)	Maximum displacement-response deviation (%)	Steady-state displacement-response deviation (%)	Settling time (%)
1000	40.10	0.00	59.90
2000	40.38	0.00	59.62
3000	37.26	0.00	62.74

Settling time governed approximately 60–63% of the boundary arc length across the three loads, compared with approximately 37–40% for maximum displacement-response deviation. Steady-state displacement-response deviation governed no main boundary segment (Table 11).

4.2 Effect of failure threshold variations on degradation-state boundaries

Failure-threshold sensitivity was assessed around the baseline thresholds of 6 mm, 3 mm, and 6.5 s for maximum displacement-response deviation, steady-state displacement-response deviation, and settling time, respectively. Each threshold was tightened or relaxed by 5% individually, while the others were held constant. The three sets of threshold values were 5.7, 6.0, and 6.3 mm; 2.85, 3.00, and 3.15 mm; and 6.175, 6.500, and 6.825 s, respectively. The main acceptable degradation domains and their boundaries were re-extracted under loads of 1000, 2000, and 3000 N, as shown in Fig. 12.

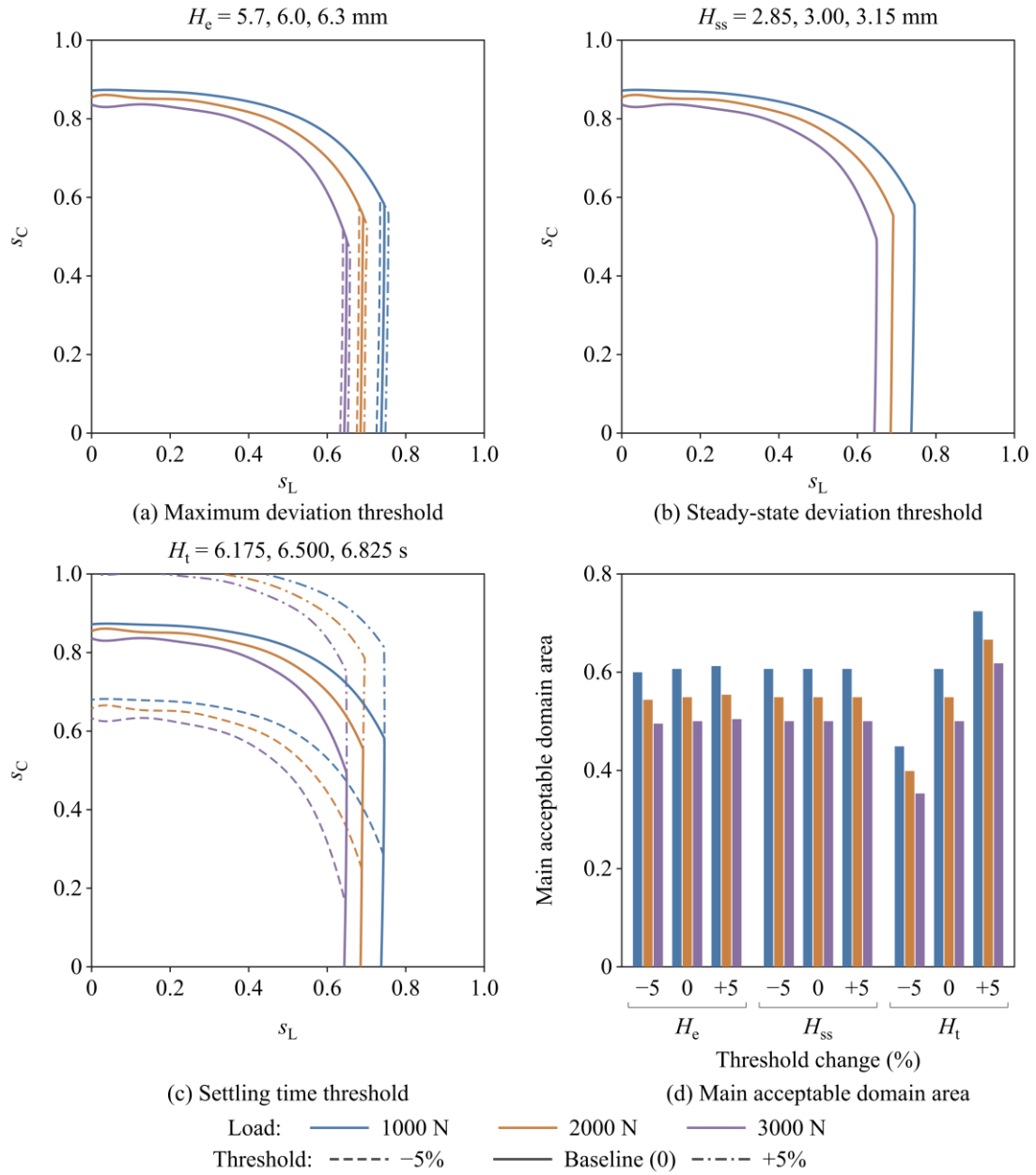


Fig. 12 Changes in the main composite degradation-state boundaries under different failure thresholds

In Fig. 12, tightening or relaxing the maximum displacement-response deviation threshold shifts its governing boundary segments toward lower or higher pump leakage degradation levels, respectively. Other governing segments change little. Varying the steady-state displacement-response deviation threshold from 2.85 to 3.15 mm produces no appreciable change in the main composite boundary. In contrast, changing the settling-time threshold alters both its governing boundary segments and their transition points with segments governed by maximum displacement-response deviation.

To compare the effect of threshold changes, domain area was expressed as a percentage change from the area at the baseline thresholds for each load (Table 12).

Table 12 Relative changes in main acceptable degradation domain area with the failure thresholds

Load (N)	H_e tightened (%)	H_e relaxed (%)	H_{ss} tightened (%)	H_{ss} relaxed (%)	H_{t_s} tightened (%)	H_{t_s} relaxed (%)
1000	−1.096	+0.97	0.000	0.000	−25.98	+19.37
2000	−0.960	+0.91	0.000	0.000	−27.38	+21.36
3000	−0.996	+0.84	0.000	0.000	−29.43	+23.51

Tightening the settling-time threshold by 5% reduced the main acceptable degradation domain area by 25.98%, 27.38%, and 29.43% at the three loads, respectively. Relaxing that threshold increased the areas by 19.37%, 21.36%, and 23.51%. Changing the maximum displacement-response deviation threshold changed area by approximately 1%. Varying the steady-state displacement-response deviation threshold over 2.85–3.15 mm did not change the main domain area (Table 12).

These differences depend on which constraints govern the boundary, the length of their governed segments, and the local performance gradients. On a segment governed by one constraint at a given load, the boundary lies where the corresponding metric equals its threshold. If that metric changes slowly with degradation near the boundary, a small threshold change can shift the boundary substantially and alter domain area. A steeper local gradient produces a smaller displacement of the boundary.

4.3 Validation of composite performance boundaries and task-state assessment

Boundary location was evaluated on five sections at fixed levels of controller degradation for each load of 1000, 2000, and 3000 N, giving 15 sections in total. The GPR boundary defined a local search range. AMESim simulations and the task failure criterion then identified the last acceptable state and the first unacceptable state on each section. A state-transition interval was found on all 15 sections, with a mean width of 0.00225 and a maximum width of 0.00250.

The midpoint of the AMESim state-transition interval served as the reference position. The absolute difference between the predicted and reference boundary positions was calculated as

$$d_i = \left| p_i - \frac{a_i + b_i}{2} \right| \tag{26}$$

Here, p_i is the GPR-predicted boundary location, while a_i and b_i are the last acceptable and first unacceptable locations identified by AMESim, respectively. The state-transition interval width represents the numerical search resolution of the reference location. Table 13 summarizes the boundary-location errors under different loads. Fig. 13 compares the GPR-predicted boundaries with the AMESim state-transition intervals.

Table 13 Boundary location errors at each load

Load (N)	Sections	Mean interval width	Mean absolute deviation	RMSE
1000	5	0.002500	0.002750	0.003666
2000	5	0.002000	0.000750	0.001186
3000	5	0.002250	0.005625	0.006829
Total	15	0.002250	0.003042	0.004527

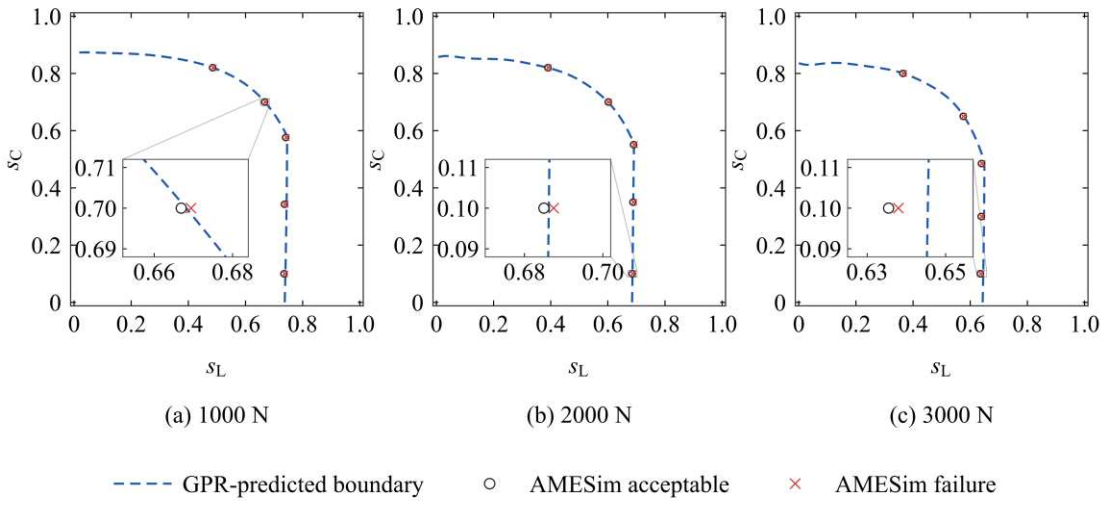


Fig. 13 Comparison of GPR-predicted boundaries and AMESim state-transition intervals

Fig. 13 and Table 13 show a boundary-location RMSE of 0.004527 across the 15 cross-sections. The error was smallest under 2000 N and largest under 3000 N. Under 3000 N, the GPR-predicted boundaries for all five validation cross-sections were shifted toward higher pump leakage degradation levels. Some AMESim-unacceptable states lay on the acceptable side of the predicted boundary, indicating a tendency to overestimate allowable degradation under high loads. This discrepancy may be associated with the greater influence of leakage losses at high loads and GPR approximation errors for nonlinear responses near the critical boundary.

Seven degradation combinations across the three loads were tested on the bench to evaluate task states under representative multi-source degradation. The three performance metrics were extracted using the calibrated leakage settings, the controller degradation parameter settings, and the evaluation method described above. Table 14 gives the measurements and classifications.

Table 14 Measured EHA task performance under representative degradation conditions

Case	Load (N)	s_L	s_C	e_{max} / Mm	e_{ss} / Mm	t_s / s	Bench state	GPR state
S1	1000	0.6401	0.10	3.943	0.147	5.77	Acceptable	Acceptable
S2	1000	0.7247	0.10	5.982	0.206	5.96	Acceptable	Acceptable
S3	2000	0.6401	0.10	4.765	0.175	5.91	Acceptable	Acceptable
S4	2000	0.7247	0.10	7.264	0.257	6.17	Unacceptable	Unacceptable
S5	3000	0.6401	0.10	5.561	0.202	6.03	Acceptable	Acceptable
S6	3000	0.7247	0.10	8.464	0.318	6.32	Unacceptable	Unacceptable
S7	2000	0.6401	0.70	4.769	0.652	6.61	Unacceptable	Unacceptable

At $s_C = 0.10$, increasing s_L from 0.6401 to 0.7247 left both cases acceptable at 1000 N. At 2000 and 3000 N, the state changed from acceptable to unacceptable because maximum displacement-response deviation exceeded its threshold (Table 14). At 2000 N and s_L = 0.6401, increasing s_C from 0.10 to 0.70 left maximum displacement-response deviation nearly unchanged, while settling time rose from 5.91 to 6.61 s and exceeded its threshold. Thus, in the S3/S4 and S3/S7 comparisons, reduced hydraulic flow delivery capability and reduced controller proportional gain caused the EHA to fail the task through different limits: maximum displacement-response deviation and settling time, respectively. This agrees with the finding that the two constraints govern distinct segments of the composite performance boundary.

The degradation parameters of the seven bench conditions were mapped onto the GPR-predicted composite performance margin distributions. This comparison establishes the positions of the measured task states relative to the predicted acceptable degradation domains, as shown in Fig. 14.

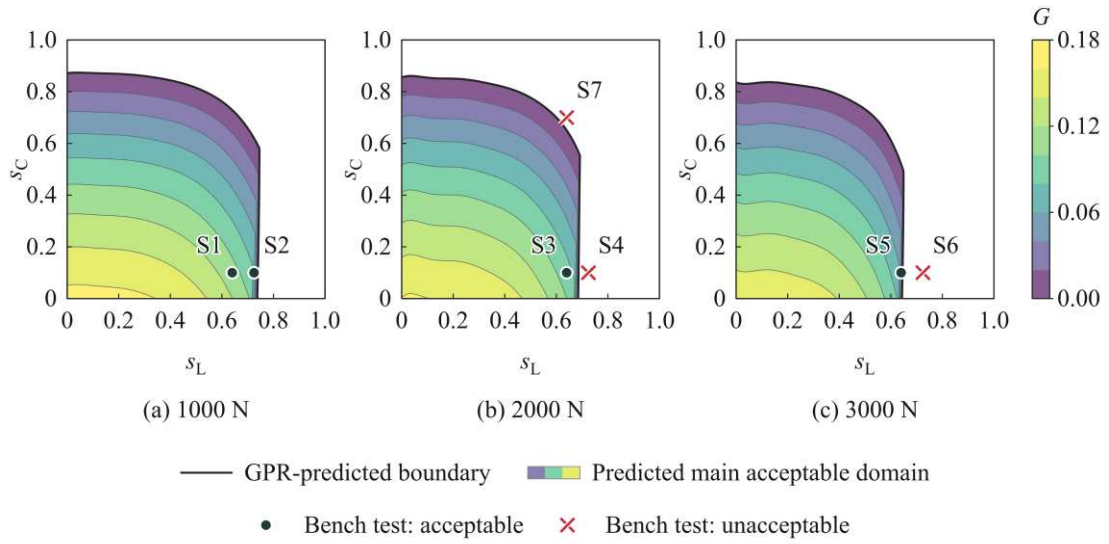


Fig. 14 EHA composite performance margin distributions and experimental task-state validation under representative degradation conditions

In Fig. 14, all four bench conditions classified as acceptable lie within the GPR-predicted main acceptable degradation domains, while the three unacceptable conditions lie outside. The distribution of the bench conditions in the degradation-state space agrees with the task-state classification based on the predicted composite boundaries.

Table 15 compares the measured and predicted composite performance margins for the seven cases.

Table 15 Composite performance margins predicted by GPR and measured on the test bench

Case	G_{test}	G_{GPR}	$\lvert\Delta G\rvert$
S1	0.112	0.108	0.005
S2	0.003	0.063	0.060
S3	0.091	0.088	0.003
S4	-0.211	-0.205	0.005
S5	0.072	0.027	0.045

Case	G_{test}	G_{GPR}	$\lvert \Delta G \rvert$
S6	-0.411	-0.623	0.212
S7	-0.017	-0.011	0.006

The predicted and measured margins had the same sign in all seven cases, but their magnitudes differed (Table 15). For S2 the measured margin was 0.003, close to the failure boundary, whereas the predicted margin was 0.063. S6 had the largest absolute difference, 0.212. The model correctly classified the selected task states, but errors remained in the predicted composite performance margins.

5 Conclusions

AMESim simulations and GPR were used to map multiple degradation parameters and task load to actuator-level performance under the prescribed EHA task. Joint performance constraints identified the main acceptable degradation domain, whose boundary was analyzed and validated. The principal findings are as follows.

(1) Pump leakage and controller proportional-gain degradation have different effects on EHA performance. Pump leakage primarily affects maximum displacement-response deviation, whereas reduced proportional gain has a stronger effect on settling time. External load modifies both relationships. The GPR models captured the nonlinear performance maps over the parameter ranges examined and provided a basis for boundary identification under multi-source degradation.

(2) Maximum displacement-response deviation and settling time governed approximately 37–40% and 60–63% of the main boundary arc length, respectively. Steady-state displacement-response deviation governed no segment. Increasing the load from 1000 to 3000 N reduced the main acceptable degradation domain area by 17.5%. Of the threshold changes examined, the settling-time threshold had the largest effect on area: tightening it by 5% reduced area by approximately 26–29%. The different task requirements therefore placed substantially different limits on acceptable degradation.

(3) Across 15 AMESim sections, the RMSE between the predicted boundary locations and the state-transition interval midpoints was 0.0045. All seven bench classifications agreed with the GPR predictions. The model thus captured the principal performance limitations under the prescribed test conditions. At 3000 N, however, the model tended to overestimate the allowable pump leakage degradation level, and performance margin errors were appreciable in some near-critical cases. More accurate assessment of critical states remains necessary.

The governing constraints can guide preventive inspection. When maximum displacement-response deviation approaches its threshold, hydraulic flow delivery capability merits priority. When settling time approaches its threshold, inspection can focus on closed-loop control authority. Because both degradation sources affect more than one metric, a single metric cannot identify the cause of a fault. The results apply to the EHA configuration studied, the prescribed reciprocating task, and the three constant loads. Application to another EHA or to flight mission acceptance requires separate qualification. Future work could examine how the boundaries change with mission conditions using dynamic loads and in-service degradation data.

References

[1] Zeng S, Chen K, Zhao S, Huangfu Y, Lan T (2025) A comparative study of three TVC actuators for a launch vehicle block. Missiles and Space Vehicles (4):1–17. https://doi.org/10.7654/j.issn.2097-1974.20250401

[2] Du S, Zhou J, Hong J, Zhao H, Ma S (2024) Application and progress of high-efficiency electro-hydrostatic actuator technology with energy recovery: a comprehensive review. Energy Conversion and Management 321:119041. https://doi.org/10.1016/j.enconman.2024.119041

[3] Fan S, Wang S, Wang Q, Wang X, Liu D, Wu X (2025) Cumulative thermal coupling modeling and analysis of oil-immersed motor-pump assembly for electro–hydrostatic actuator. Chinese Journal of Aeronautics 38(5):103250. https://doi.org/10.1016/j.cja.2024.09.026

[4] Jia Z, Li Z, Wang K, Zhi G, Liu Z, Vong CM (2026) Graph convolutional contrastive learning for few-shot open-set fault diagnosis in electro-hydrostatic actuators. IEEE Trans Aerosp Electron Syst 62:3076–3092. https://doi.org/10.1109/taes.2025.3644834

[5] Zhao X, Zhu X, Liu J, Hu Y, Gao T, Zhao L, Yao J, Liu Z (2024) Model-assisted multi-source fusion hypergraph convolutional neural networks for intelligent few-shot fault diagnosis to electro-hydrostatic actuator. Information Fusion 104:102186. https://doi.org/10.1016/j.inffus.2023.102186

[6] He X, Zhao C, Li S, Zhao X, Yang X, Song Y, Yao J (2025) Diffusion-enhanced dual-domain adversarial network: a zero-shot fault diagnosis method for electrohydrostatic actuators. IEEE Trans Instrum Meas 74:3553709. https://doi.org/10.1109/tim.2025.3595601

[7] He X, Hu Y, Zhang S, Song Y, Zhao X, Yao J (2026) Deep-learning-based multicondition transfer diagnosis of compound faults in electrohydrostatic actuator. IEEE Internet Things J 13(11):22959–22972. https://doi.org/10.1109/jiot.2026.3668433

[8] Yan W, Jia Z, Liu Z, Wang S, Zhang W, Wang K (2026) Vibration-sensor-free diagnosis for aviation piston pumps: a CWT-ViT approach with high-dimensional tensor fusion. Measurement 258:119050. https://doi.org/10.1016/j.measurement.2025.119050

[9] Xu D, Feng Z, Sui S, Lin YH (2019) Reliability assessment of electrohydraulic actuation control system subject to multisources degradation processes. IEEE/ASME Trans Mechatron 24(6):2594–2605. https://doi.org/10.1109/tmech.2019.2953333

[10] Sun M, Fu J, Wang C, Wu H, Zhao Z, Wang W, Bai L (2026) System-level modeling and preliminary experiment study of a redundant EHA for more electric helicopter flight control. Chinese Journal of Aeronautics 39(9):103891. https://doi.org/10.1016/j.cja.2025.103891

[11] Ma Z, Liao H, Gao J, Nie S, Geng Y (2023) Physics-informed machine learning for degradation modeling of an electro-hydrostatic actuator system. Reliability Engineering & System Safety 229:108898. https://doi.org/10.1016/j.ress.2022.108898

[12] Zhang J, Li X, Lyu F, Schlegel F, Schmitz K, Liu S, Huang W, Xu B (2025) Critical operation range of electro-hydrostatic actuator pumps based on cylinder block tilting states. Chinese Journal of Aeronautics 38(12):103382. https://doi.org/10.1016/j.cja.2024.103382

[13] Tang J, Chen H, Liu H, Zhang P, Xu M, Tao H, Liu N, Feng S, Qian J (2026) Performance degradation indicator construction for EHA leakage faults under variable load disturbances. Journal of Mechanical & Electrical Engineering. Published online 13 May 2026. https://link.cnki.net/urlid/33.1088.TH.20260513.1004.006

[14] Feng S, Chen H, Tang J, Zhang P, Liu H, Tao H, Chen R, Fei X (2026) Anti-load performance evaluation method for electro-hydrostatic actuators based on physics-embedded attention mechanism. Mechanical Systems and Signal Processing 258:114741. https://doi.org/10.1016/j.ymssp.2026.114741

[15] Voßwinkel R, Pyta L, Schrödel F, Mutlu İ, Mihailescu-Stoica D, Bajcinca N (2019) Performance boundary mapping for continuous and discrete time linear systems. Automatica 107:272–280. https://doi.org/10.1016/j.automatica.2019.05.055

[16] Ranjan P, Bingham D, Michailidis G (2008) Sequential experiment design for contour estimation from complex computer codes. Technometrics 50(4):527–541. https://doi.org/10.1198/004017008000000541

[17] Bichon BJ, Eldred MS, Swiler LP, Mahadevan S, McFarland JM (2008) Efficient global reliability analysis for nonlinear implicit performance functions. AIAA Journal 46(10):2459–2468. https://doi.org/10.2514/1.34321

[18] Echard B, Gayton N, Lemaire M (2011) AK-MCS: an active learning reliability method combining Kriging and Monte Carlo simulation. Structural Safety 33(2):145–154. https://doi.org/10.1016/j.strusafe.2011.01.002

[19] Bichon BJ, McFarland JM, Mahadevan S (2011) Efficient surrogate models for reliability analysis of systems with multiple failure modes. Reliability Engineering & System Safety 96(10):1386–1395. https://doi.org/10.1016/j.ress.2011.05.008

[20] Yan H, Yan P, Zhou C, Yu C, Du J (2026) System reliability analysis with active learning: a one-step look-ahead policy based on expected uncertainty reduction function. Reliability Engineering & System Safety 274:112397. https://doi.org/10.1016/j.ress.2026.112397

[21] Dong B, Lu Z (2022) Efficient adaptive Kriging for system reliability analysis with multiple failure modes under random and interval hybrid uncertainty. Chinese Journal of Aeronautics 35(5):333–346. https://doi.org/10.1016/j.cja.2021.08.017

[22] Xu C, Yang Y, Wu H, Zhou J (2023) A new active learning method for system reliability analysis with multiple failure modes. Reliability Engineering & System Safety 240:109614. https://doi.org/10.1016/j.ress.2023.109614

[23] Wu M, Chen H, Tai M, Xiahou T, Ge Z, Liu Z, Chu B, Zhao Z, Liu Y (2024) Active learning-based metamodeling for hybrid uncertainty quantification of hydro-mechatronic-control systems: a case study of EHA systems. Chinese Journal of Aeronautics 37(12):12–30. https://doi.org/10.1016/j.cja.2024.08.023